

# Internal Gravity Wave Breaking in White Dwarf Binaries

Yubo Su,<sup>1</sup> Daniel Lecoanet,<sup>2</sup> Dong Lai,<sup>1</sup>

<sup>1</sup> *Cornell Center for Astrophysics and Planetary Science, Department of Astronomy, Cornell University, Ithaca, NY 14853, USA*

<sup>2</sup> *Princeton Center for Theoretical Science, Princeton University, Princeton, NJ 08544, USA*

Accepted XXX. Received YYY; in original form ZZZ

## ABSTRACT

In sufficiently compact white dwarf binaries, dynamical tides raise a train of internal gravity waves that propagate towards the surface. We perform 2D numerical simulations of these waves undergoing nonlinear wave breaking in an incompressible, isothermal atmosphere. After an initial transient phase, we find that these waves induce a sharp transition between a non-rotating core and synchronously rotating envelope. We find evidence that the width of this transition layer is bound from below by the Kelvin-Helmholtz Instability. We provide analytical formulae for absorption and reflection of incident waves off the critical layer up to prefactors of order unity. These prefactors converge to constant values when artificial dissipation is decreased. We provide dimensionless criteria necessary to resolving momentum transfer within the critical layer. Finally, we speculate on the application of our model to tidal synchronization and heating in astrophysical systems.

**Key words:** white dwarfs – hydrodynamics – binaries:close – waves

## 1 INTRODUCTION

[Below copied from proposal, will rewrite]

Compact white dwarf (WD) binary systems, with orbital periods in the range of minutes to hours, are important for a range of astrophysical problems. They are the most important sources of gravitational waves (GWs) for the Laser Interferometric Space Antenna (LISA) (Nelemans 2009). They are also thought to produce interesting optical transients such as underluminous supernovae (Perets et al. 2010), Ca-rich fast transients (García-Berro et al. 2017), and tidal novae (Fuller & Lai 2012b). Most importantly, they have been proposed as the likely progenitors of type Ia supernovae (e.g. Iben Jr & Tutukov 1984; Webbink 1984) or more recently (Gilfanov & Bogdán 2010; Maoz et al. 2010). While presently only a few tens of compact WD binaries are known (Korol et al. 2017), *Gaia* (currently gathering data) is expected to expand the catalog to a few hundreds (Korol et al. 2017) (results based on *Gaia*’s second data release have already begun to appear (Shen et al. 2018; Kilic et al. 2018)), and the Large Synoptic Survey Telescope (LSST, first light scheduled for 2020) will likely detect a few thousand more (Korol et al. 2017). These observations will significantly advance the understanding of WD binaries and their evolution. My proposed theoretical and computational research is well-timed to take advantage of these new advances.

In spite of the broad importance of WD binaries, the evolution of these systems prior to their final mergers is not well understood. Much of this uncertainty comes from our imprecise understanding of tidal interactions, which play an important role during a compact WD binary’s inspiral (Fuller & Lai 2012a). Previous studies have shown that these interactions manifest as tidal excitation of internal gravity waves (IGW), waves in the WD fluid restored by the

buoyancy force due to density stratification (Fuller & Lai 2011). As these waves propagate outwards towards the WD surface, they grow in amplitude until they break, as do ocean waves on a shore, and transfer both energy and angular momentum from the binary orbit to the outer envelope of the WD (Fuller & Lai 2011, 2012a).

Previous works have found that the dissipation of IGW can generate significantly more energy than thermal radiation from the isolated WD surface and is thus a major contributor to the WD energy budget (Fuller & Lai 2012a, 2013). However, these works parameterized the wave breaking process in an ad hoc manner. The details of dissipation, namely the location and spatial extent of the wave breaking, affect the observable outcome: dissipation near the surface of the WD can be efficiently radiated away and simply brightens the WD, while dissipation deep in the WD envelope causes an energy buildup that results in energetic flares (Fuller & Lai 2012b). Works in other fields based on numerical simulations show that strongly nonlinear wave breaking behaves differently than predictions based in linear and weakly nonlinear theory (Winters & D’Asaro 1994; Barker & Ogilvie 2010). Such fully nonlinear numerical simulations have not been performed for WDs.

In Section 2, we will describe the system of equations we will use to analyze IGW breaking. In Section 3, we discuss relevant analytical results. In Section 5 we present the results of numerical simulations. Finally, in Section 6 we discuss the results of the preceeding section.

## 2 PROBLEM DESCRIPTION

We consider a two-dimensional incompressible, isothermal fluid, representative of degenerate matter in WDs. We furthermore ne-

glect temperature variations and assume a barotropic equation of state  $P(\rho, T) = P(\rho)$  as a first approximation. As we are interested in dynamics far from the center of the WD, we approximate the gravitational field as uniform. We model the background density stratification as  $\rho_0(x, z) = \rho_0(z) = \rho_0(z=0)e^{-z/H}$  for some reference density  $\rho_0(z=0) = \rho_0(z)|_{z=0}$ .

The Euler equations for an incompressible, barotropic fluid in a uniform gravitational field are

$$\vec{\nabla} \cdot \vec{u}_1 = 0, \quad (1a)$$

$$\frac{D\rho}{Dt} = 0, \quad (1b)$$

$$\frac{D\vec{u}_1}{Dt} + \frac{\vec{\nabla}P}{\rho} + g\hat{z} = 0. \quad (1c)$$

$\frac{D}{Dt} = \frac{\partial}{\partial t} + (\vec{u}_1 \cdot \vec{\nabla})$  is the Lagrangian or material derivative, and  $\vec{u}_1, \rho, P$  denote the velocity field, density and pressure respectively. We denote  $-g\hat{z}$  constant gravitational acceleration. Note that at hydrostatic equilibrium  $\frac{\partial}{\partial t} = 0$  we have  $\vec{\nabla}P_0 = -\rho_0 g\hat{z}$  and so  $P_0 = \rho_0 gH$ . A shear flow of form  $\vec{u}_1 = u_{1x}(x, z, t)\hat{x} = u_{1x}(z)\hat{x}$  is permitted in hydrostatic equilibrium, but we will assume no background shear flow. Physically, this assumption corresponds to a non-rotating star, or going to the corotating frame of a rigidly rotating star.

In practice, it is convenient to introduce coordinate  $\Upsilon = \ln \frac{\rho}{\rho_0}$ . This both identically enforces  $\rho > 0$  and avoids numerical issues in the  $\frac{\vec{\nabla}P}{\rho}$  term if  $\rho$  is small. We also define reduced pressure  $P = \frac{P}{\rho}$ . Then, we may rewrite the second two equations of Equation 1 as

$$\frac{D\Upsilon}{Dt} + u_{1z} \frac{\partial \ln \rho_0}{\partial z} = 0, \quad (2a)$$

$$\frac{D\vec{u}_1}{Dt} + \vec{\nabla}P + P\vec{\nabla}\Upsilon + g\hat{z} = 0. \quad (2b)$$

Note that in the new coordinates, hydrostatic equilibrium corresponds to  $\Upsilon_0 = 1, P_0 = gH$ .

### 3 INTERNAL GRAVITY WAVES: THEORY

#### 3.1 Analytical Properties: Linear

In the small perturbation limit, where flow velocities are small compared to the characteristic space and time scales  $\frac{\partial}{\partial t} \gg \vec{u}_1 \cdot \vec{\nabla}$ , we may linearize Equation 2. We ignore the advective components of the material derivative and consider small deviations  $\Upsilon_1 = \Upsilon - \Upsilon_0, P_1 = P - P_0$  about hydrostatic equilibrium:

$$\vec{\nabla} \cdot \vec{u}_1 = 0, \quad (3a)$$

$$\frac{\partial \Upsilon_1}{\partial t} - \frac{u_z}{H} = 0, \quad (3b)$$

$$\frac{\partial \vec{u}_1}{\partial t} + \vec{\nabla}P_1 + (1 + \Upsilon_1)g\hat{z} = 0. \quad (3c)$$

This can be solved to obtain solutions up to undetermined amplitude  $A$  the well-known result (Drazin 1977; Dosser & Sutherland 2011b):

$$u_{1z}(x, z, t) = Ae^{z/2H} e^{i(k_{1x}x - k_{1z}z - \omega_1 t)}, \quad (4)$$

where  $\omega_1$  satisfies dispersion relation

$$\omega_1^2 = \frac{N^2 k_{1x}^2}{k_{1x}^2 + k_{1z}^2 + \frac{1}{4H^2}}, \quad (5)$$

where

$$N^2 \equiv g^2 \left( \frac{d\rho}{dP} - \frac{\partial \rho}{\partial P} \Big|_{ad} \right) = \frac{g}{H}, \quad (6)$$

the Brunt-Väisälä frequency is constant. Our sign convention is such that a wave with  $k_{1x}, k_{1z} > 0$  has positive vertical group velocity (see Equation 8).

In the weak stratification limit  $k_{1z}H \gg 1$ , the solution exhibits the following characteristics:

- The amplitude of the wave grows with  $z$  as  $e^{z/2H}$ . Thus, the linear approximation is always violated for sufficiently large  $z$ .
- The phase and group velocities can be computed respectively:

$$\vec{c}_{ph} = (k_{1x}\hat{x} - k_{1z}\hat{z}) \frac{\omega_1}{k_{1x}^2 + k_{1z}^2 + \frac{1}{4H^2}}, \quad (7)$$

$$\vec{c}_g = N \frac{\left( k_{1z}^2 + \frac{1}{4H^2} \right) \hat{x} + (k_{1x}k_{1z}\hat{z})}{\left( k_{1x}^2 + k_{1z}^2 + \frac{1}{4H^2} \right)^{3/2}}. \quad (8)$$

We note  $\vec{c}_{ph} \cdot \vec{c}_g = +O\left(\frac{1}{(k_{1z}H)^2}\right) \approx 0$ , the usual result (e.g. (Drazin 1977; Dosser & Sutherland 2011a)). Note again that  $c_{gz} > 0$  for  $k_{1x}, k_{1z} > 0$ , a consequence of our sign choice in Equation 4.

- The time-averaged total  $x$ -momentum flux carried in the  $\hat{z}$  direction can be computed. Since the linear solution is separable as  $f(x, z, t) = f(z)e^{i(k_{1x}x - \omega_1 t)}$ ,  $x$  averaging and time averaging are equivalent, so we may write

$$S \equiv \langle \rho u_{1x} u_{1z} \rangle_x \equiv \frac{1}{L_x} \int_0^{L_x} \rho u_{1x} u_{1z} dx, \quad (9)$$

$$\approx -\frac{A^2}{2} \rho_0(z=0) \frac{k_{1z}}{k_{1x}}, \quad (10)$$

where  $\langle \dots \rangle_x$  denotes  $x$ -averaging.

#### 3.2 Wave Generation: Analytical Analysis

Since we are only concerned with the behavior of the wave at high  $z$  where wave breaking occurs, we generate waves in the most numerically convenient way. As long as physically representative IGW are generated and wave dynamics are only examined far from the forcing region, the exact excitation mechanism is not important for our conclusions.

To model continuous excitation of IGWs deep in the WD interior propagating towards the surface, we use a volumetric forcing term to excite IGW near the bottom of the simulation domain<sup>1</sup>. Our forcing excites both IGWs propagating upwards, imitating a wave tidally excited deeper in the WD, and downwards, which are damped away by the damping layers described in subsection 4.2.

As not to interfere with the incompressibility constraint, we force the system on the density equation. This constitutes replacing Equation 2a with

$$\frac{D\Upsilon}{Dt} + u_{1z} \frac{\partial \ln \rho_0}{\partial z} = F e^{-\frac{(z-z_0)^2}{2\sigma^2}} \cos(k_{1x}x - \omega_1 t). \quad (11)$$

Using a narrow Gaussian profile excites a broad  $k_z$  wavenumber spectrum, and only the  $k_{1z}$  satisfying dispersion relation Equation 5 for the given  $k_{1x}, \omega_1(k_{1x}, k_{1z})$  will propagate.

<sup>1</sup> Interfacial forcing is numerically unstable when using a Chebyshev polynomial basis in the  $z$  direction and impossible when using a Fourier basis.

In the linearized system, the effect of this forcing can be solved analytically up to good accuracy: we first approximate the driving term using  $e^{-\frac{(z-z_0)^2}{2\sigma^2}} \approx \sqrt{2\pi\sigma^2}\delta(z-z_0)$ , the  $\sigma \rightarrow 0$  limit<sup>2</sup>. This system is solved exactly by matching the two homogeneous solutions above and below  $z_0$ . We may then approximately relax the solution to nonzero  $\sigma$ : an extra factor of  $e^{-\frac{(k_{1z}\sigma)^2}{2}}$  arises compared to the  $\delta$ -function solution (evaluating the Fourier Transform of  $e^{-\frac{(z-z_0)^2}{2\sigma^2}}$  at  $k_z = k_{1z}$ ), and we obtain

$$u_z(x, z, t) = \frac{Fgk_{1x}^2}{\omega_1^2} \frac{1}{2ik_{1z}} \frac{e^{-\frac{(k_{1z}\sigma)^2}{2}}}{\sqrt{2\pi\sigma^2}} \times \begin{cases} e^{\frac{z-z_0}{2H}} e^{i(k_{1x}x + k_{1z}(z-z_0) - \omega_1 t + \frac{1}{2k_{1z}H})} & z > z_0 \\ e^{\frac{z-z_0}{2H}} e^{i(k_{1x}x - k_{1z}(z-z_0) - \omega_1 t + \frac{1}{2k_{1z}H})} & z < z_0 \end{cases}. \quad (12)$$

The  $z > z_0$  solution models an upwards-propagating IGW wave-train inbound on the simulation domain from below. The solution for  $u_{1x}(x, z, t)$  can be obtained analytically from incompressibility Equation 1a.

### 3.3 Wave Breaking Location

In developing the results above, we have neglected advective terms  $\frac{\partial}{\partial t} \gg \vec{u}_1 \cdot \vec{\nabla}$ . However, since  $|\vec{u}_1| \propto e^{z/2H}$ , any nonzero amplitude IGW will eventually violate the linearity criterion. This regime is relevant in practice since the IGW may grow to nonlinear amplitudes before it reaches the surface of the WD (Fuller & Lai 2011, 2012a). We can coarsely estimate the height at which this happens by when the Lagrangian displacement  $\vec{\xi} = \frac{\vec{u}_1}{i\omega}$  of a fluid parcel satisfies

$$\vec{\xi} \cdot \vec{k}_1 \gtrsim 1. \quad (13)$$

Another useful result quantifies the wave-induced mean flow (Andrews & McIntyre 1976; Dosser & Sutherland 2011b):

$$\langle u_{1x} \rangle \equiv \bar{U} = \frac{1}{L_x} \int u_{1x} dx = \frac{\langle u_{1x} u_{1z} \rangle_x}{c_{g,z}}, \quad (14)$$

This formula is analogous to Stokes' drift for surface waves and can be derived by considering the propagation of  $S$  (Equation 9) into a medium at rest. Solving for  $\bar{U} = c_{ph,x}$  the critical layer condition (see subsection 3.4 immediately below), we recover  $\frac{u_{1x}k_{1x}}{\omega} = \xi_x k_{1x} \sim 1$ , roughly equivalent to the nonlinearity criterion Equation 13. This condition predicts where the wave's self-acceleration alone is sufficient to induce critical layer absorption.

### 3.4 Formation and Dynamics of Critical Layer

[TODO rewrite more clearly, it's just copy pasted together right now]

The general understanding of nonlinear IGW breaking is that the waves' interactions with the mean flow of the fluid transfer horizontal momentum from the waves into the fluid; such a process has been conjectured to be responsible for tidal synchronization in stellar binaries (Zahn 1975; Goldreich & Nicholson 1989) as well as the quasi-biennial oscillation (Lindzen & Holton 1968). The details of this process have been laid out in a few key papers: IGWs

are globally unstable to resonant three-wave interactions (Drazin 1977), causing energy transfer out of the IGW to daughter modes. These steeper daughter modes facilitate wave breaking, depositing horizontal momentum in the fluid's mean flow (Klostermeyer 1991).

In accordance with literature and the simulation setup, we will assume momentum redistribution is inefficient (see subsection 6.1 for analysis of this assumption). The mean flow will then grow in place until it reaches the horizontal phase velocity of the parent IGW. Then, a critical layer forms at which the frequency of the incident IGW is Doppler-shifted to zero. The interaction of the parent IGW with the mean flow was first studied in the inviscid, linear regime in (Booker & Bretherton 1967), which found nearly complete absorption. This result was reproduced with nonzero viscosity (Hazel 1967), but weakly nonlinear theory (Brown & Stewartson 1982) and fully nonlinear simulations (Winters & D'Asaro 1994) suggest that nonlinear effects can induce reflection.

A purely horizontal shear flow  $\bar{U}(z)\hat{x}$  can be seen in Equation 1 to have the effect of modifying time derivatives  $\partial_t$  to their frequency in the comoving frame of the fluid  $\partial_t - \bar{U}(z)\partial_x$ . For a critical value  $\omega_1 - \bar{U}_c k_{1x} = 0$ , the frequency of the linear wave in the fluid's frame of reference vanishes and critical behavior is observed. In a linear (Booker & Bretherton 1967) or viscous (Hazel 1967) theory, the incident wave has amplitude reflection and transmission coefficients

$$\text{Ri} \equiv \frac{N^2}{\left(\frac{\partial \bar{U}}{\partial z}\right)^2} \bigg|_{z_c}, \quad (15)$$

$$\mathcal{R} = e^{-2\pi\sqrt{\text{Ri}-\frac{1}{4}}}, \quad \mathcal{T} = e^{-\pi\sqrt{\text{Ri}-\frac{1}{4}}}, \quad (16)$$

where we have defined local Richardson number Ri at the critical layer  $z_c : \bar{U}(z_c) = \frac{\omega_1}{k_{1x}}$ . In the  $\text{Ri} \gg 1$  limit,  $\mathcal{R}, \mathcal{T} \ll 1$  and the incident wave is completely absorbed to good approximation.

When the fluid absorbs the incident wave, it absorbs the incident horizontal momentum flux as well, which is converted into additional horizontal momentum of the shear flow. Since the shear flow cannot exceed  $\bar{U}_c$  the horizontal phase velocity of the incident wave, the critical layer must instead propagate downwards to accommodate the incident momentum. The total horizontal momentum of the shear flow then obeys conservation equation

$$\frac{\partial}{\partial t} \int_0^{L_z} \rho(z) \bar{U}(z, t) dz + \Delta S = 0. \quad (17)$$

We define  $\Delta S$  to be the change in flux across the critical layer, or equivalently the negative of the absorbed flux. Treating  $\bar{U}(z > z_c) = \bar{U}_c$ ,  $\bar{U}(z < z_c) = 0$  gives us exactly

$$\rho(z_c) \bar{U}_c \frac{\partial z_c}{\partial t} = \Delta S(z_c(t)). \quad (18)$$

$\Delta S(z_c)$  denotes the change in  $S$  across  $z_c$ . For constant  $\Delta S$  in time and  $\rho \approx \rho_0$ , this has analytical solution

$$z_c(t) = -H \ln t - H \ln \frac{H\rho_0(z=0)c_{ph,x}}{-\Delta S}. \quad (19)$$

Note that constant  $-\Delta S$  corresponds physically to the picture where constant  $S$  carried by the IGWs, given by Equation 10, is fully absorbed at the critical layer, in which case  $\Delta S = -S$ .

<sup>2</sup> In practice,  $\sigma$  must be large enough to be numerically resolved by the spectral code.

## 4 INTERNAL GRAVITY WAVES: LINEAR NUMERICAL SIMULATION

Towards numerical simulation of IGW breaking, we first verify agreement with linear theory at weak forcing amplitudes. We perform direct numerical simulation using the pseudo-spectral code Dedalus (Burns et al. 2016). In subsection 4.1 we discuss choices of numerical parameters, in subsection 4.2 we separately discuss use of a damping zone at the top and bottom of the domain, and in subsection 4.3 we present the results of our “linear” simulations, where we solve the full nonlinear fluid equations for weak forcing.

### 4.1 Numerical Setup

We nondimensionalize by taking  $H = N = \rho_0(z = 0) = 1$  in Equation 1.

Denote  $L_x, L_z$  to be the physical dimensions of the simulation domain. Our simulation domain is smaller than our full physical domain, so we adopt reflection-suppressing boundary conditions. We use periodic boundary conditions in the  $x$  direction and damping layers (described in subsection 4.2) in the  $z$  direction to damp perturbations exiting the top and bottom of the domain. We use a Fourier basis in the  $x$  direction and either a Chebyshev or Fourier basis in the  $z$  direction; our results were robust to either set of basis functions. We varied the number of  $x, z$  modes (denoted  $N_x, N_z$  respectively), and used 3/2 dealiasing (Boyd 2001).

The geometry of our simulation domain is fixed by three parameters:  $L_x, L_z$ , and  $z_0$  the forcing location. We use  $z_0 = 0.2L_z$  to force sufficiently far from the lower damping zone and permit sufficient room for the upwards-moving wave to grow at  $\propto e^{z/2H}$ . We choose  $L_z = 10H$  to give  $\sim e^3$  amplitude growth between the damping zones. Finally, we want similar grid spacing  $\frac{L_x}{N_x} \sim \frac{L_z}{N_z}$ . For computational savings, we fix  $N_z = 4N_x$ . We use  $L_x = 4H = \frac{2}{5}L_z$ .

The time integration uses a split implicit-explicit third-order scheme where certain terms are treated implicitly and the remaining terms are treated explicitly. A third-order, four-stage DIRK-ERK scheme (Ascher et al. 1997) is used with adaptive timesteps computed from advective Courant-Friedrichs-Lewy (CFL) time. Specifically, we use  $\Delta t = 0.7 \min(\Delta x/u_x, \Delta z/u_{1z})$ , where the minimum is taken over every grid point in the domain and  $\Delta x, \Delta z$  are the grid spacings in the  $x$  and  $z$  directions respectively.

The physics of our simulation is fixed by four parameters:  $k_{1x}, \omega_1, F, \nu$ . We describe our choices for these parameters below:

- $k_{1x}$ : Astrophysical IGWs in stars are generally excited by the  $l = 2$  component of the tidal potential, for which  $k_\perp \sim \frac{1}{R}$  where  $R$  is the radius of the star. To best emulate this, we use  $k_{1x} = \frac{2\pi}{L_x}$  the smallest permitted wavenumber permitted by periodic boundary conditions.

- $\omega_1$ : We choose  $\omega_1$  by evaluating dispersion relation  $\omega_1(k_{1x}, k_{1z})$  for some desired  $k_{1z}$ .

Astrophysical IGWs also generally satisfy  $\omega \ll N$ , or equivalently  $\frac{k_r}{k_\perp} \sim k_r R \gg 1$ . Since  $H \lesssim R$ , we aim to study  $k_{1z}H \gg 1$ . However, to satisfy this well is computationally expensive:  $L_z \gg H$  is required to give waves ample room to grow within the simulation domain, but we want  $k_{1z}$  to be sufficiently separated from the grid spacing  $\sim L_z/N_z$  that nonlinear effects can be seen in later simulations (see subsection 5.1). Thus,  $N_z$  sets how well we can satisfy  $k_{1z}H \gg 1$ ; we choose  $k_{1z}H = 1$ .

- $F$ : We first choose  $F$  forcing strength such that  $\tilde{\xi} \cdot \vec{k}_1 \ll 1$  is satisfied everywhere throughout the domain. This constraints  $F$  by Equation 12.

- $\nu$ : Nonlinear effects transfer wave energy from  $\vec{k}_1$  to smaller scales. Since well-resolved simulations using spectral methods have no inherent numerical viscosity, energy will accumulate at grid scales in the absence of artificial dissipation. We introduce dissipation parameter  $\nu$  used for both artificial viscosity and artificial diffusivity. We ensure our equations of motion continue to conserve horizontal momentum (see Section A for details). Under weak forcing, we may set  $\nu = 0$ , since energy transfer out of the parent  $\vec{k}_1$  mode is negligible.

Finally, we use initial conditions  $\vec{u}(0) = \Upsilon(0) = 0, \varpi(0) = 1$  corresponding to hydrostatic equilibrium and no initial fluid motion.

### 4.2 Damping Layers

To imitate an infinite fluid using a finite simulation domain, we use periodic boundary conditions in the  $x$  direction and damping layers at the top and bottom of the  $z$  direction. This damps waves that reach the edge of the simulation domain without inducing nonphysical reflection. Specifically, these are implemented by introducing linear damping terms to Equation 2:

$$\begin{aligned} \frac{D\Upsilon}{Dt} + u_{1z} \frac{\partial \ln \rho_0}{\partial z} &= -\Gamma(z)\Upsilon, \\ \frac{D\vec{u}_1}{Dt} + \vec{\nabla}P + P\vec{\nabla}\Upsilon + g\hat{z} &= -\Gamma(z)\vec{u}_1, \\ \frac{1}{2\tau} \left[ 2 + \tanh \frac{z - z_T}{\Delta z} + \tanh \frac{z_B - z}{\Delta z} \right] &= \Gamma(z), \end{aligned} \quad (20)$$

where  $z_B = 0.05L_z, z_T = 0.95L_z$  are the boundaries of the damping zone. This strongly damps perturbations below  $z_B$  and above  $z_T$  with damping time  $\tau$ , negligibly affects dynamics between  $z_B, z_T$  and has transition width governed by  $\Delta z$ ; we use  $\Delta z = 0.025L_z$ . This prescription, used in similar studies (Lecoanet et al. 2016), has the advantage of being smooth, important for spectral methods. Further details of our implementation of the fluid equations in Dedalus are described in Section A.

### 4.3 Simulation Results

We describe the results of a simulation satisfying the parameter choices in subsection 4.1 such that  $\tilde{\xi} \cdot \vec{k}_1 \ll 1$  everywhere.

During the simulation, we expect IGW of form Equation 12 to be excited. Incompressibility allows us to compute a  $\vec{u}_1(x, z, t)$  profile analytically. The amplitude of the observed IGW in  $\vec{u}$  relative to analytical solution  $\vec{u}_1$  can be estimated with estimator  $\hat{A}(t)$

$$\hat{A}(t) = \frac{\int_{z_b}^{z_t} \int_0^{L_x} \rho_0 (k_{1x} u_x u_{1x} - k_{1z} u_{1z} u_{1z}) \, dx dz}{\int_{z_b}^{z_t} \int_0^{L_x} \rho_0 (k_{1x} u_{1x}^2 - k_{1z} u_{1z}^2) \, dx dz} \quad (21)$$

If  $\vec{u} = \vec{u}_1$  over  $z \in [z_b, z_t], \forall t$ , then it's clear that  $\hat{A}(t) = 1$ . The choice of multiplication by  $\rho_0$  is such that the integrand is of roughly equal magnitude throughout the domain of integration (as  $\vec{u} \propto e^{z/2H}$ ), while including a weighting by  $k_{1x}, k_{1z}$  ensures that reflected components with wavevector  $\vec{k} = k_{1x}\hat{x} - k_{1z}\hat{z}$  identically vanish in the  $\hat{A}$  estimator. Both of these features become important in later sections (see subsection 5.4).

For a simulation satisfying  $\tilde{\xi} \cdot \vec{k}_1 \ll 1$  everywhere, we expect  $\hat{A}(t) = 1$  so long as we consider only the domain between the forcing and damping zones, i.e.  $z_b \gtrsim z_0, z_t \lesssim z_T$  ( $z_0, z_T$  are defined

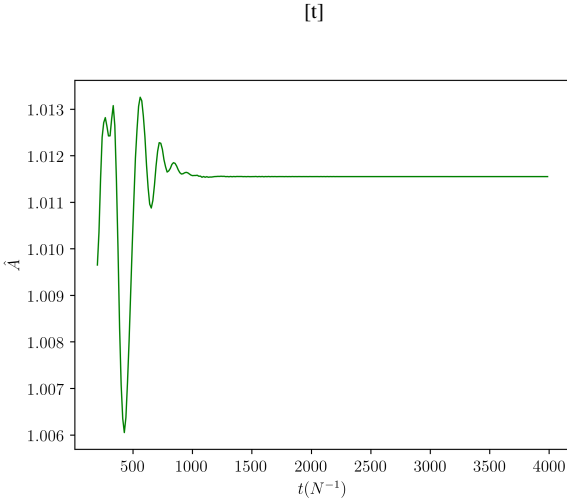


**Figure 1.** Amplitude of excited wave over time in weak forcing simulation, computed using Equation 21.  $\hat{A}(t) = 1$  corresponds to perfect agreement with the analytical estimate. After an initial transient phase, we observe great agreement with Equation 12, and in particular  $\hat{A}(t)$  asymptotes to a constant value, implying continuous excitation of identical IGW.

in Equation 11 and Equation 20 respectively). For consistency with the nonlinear case later, we choose  $z_b = z_0 + 3\sigma$ ,  $z_t = z_b + H$ , though instead using  $z_t = z_T - \Delta z$  does not change the results appreciably. The resulting measurement of  $\hat{A}(t)$  is shown in Figure 1.

A second prediction of the analytical theory is that  $S(z, t)$  should be spatially flat between the forcing and damping zone (Equation 9). We make may a slightly more accurate estimate of  $S_1$  the flux carried in the IGW by directly substituting  $\vec{u}_1$  into Equation 9. Calling this estimate  $S_1$ , we may then measure the agreement of our simulation with analytical expectation by computing

$$\hat{S}(z, t) \equiv \frac{\int_0^{L_x} \rho u_x u_z \, dx}{\int_0^{L_x} \rho_0 u_{1x} u_{1z} \, dx}. \quad (22)$$

For our weak forcing simulation,  $\hat{S} = 1$  is expected between  $z_0, z_T$ , and indeed we observe agreement with this in Figure 2.

## 5 INTERNAL GRAVITY WAVES: NONLINEAR SIMULATION

To perform simulations of wave breaking phenomena, we use the same values as subsection 4.1 except for  $F, \nu$ . In particular, we choose  $F$  such that  $\vec{k}_1 \cdot \vec{\xi} = 0.1$  in the forcing zone, which implies  $\vec{k}_1 \cdot \vec{\xi}$  is exceeded before  $z_T$  the upper damping zone. The dissipation parameter  $\nu$  was varied across the various simulations. To quantify  $\nu$ , we define Reynolds number

$$\text{Re} = \frac{LU}{\nu} \equiv \frac{\omega_1}{\nu k_{1z}^2}. \quad (23)$$

A table of our simulation viscosities can be found in Table 1.

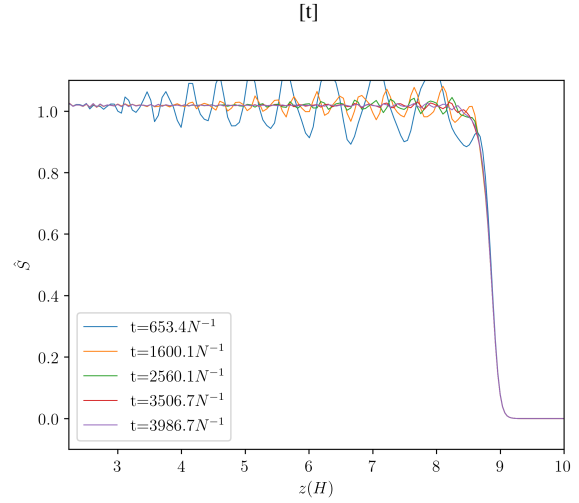


**Figure 2.** Equation 22 as a function of  $z$  at select times  $t$ . As initial transients die out,  $\hat{S}(z, t) = 1$  to very good agreement below  $z \lesssim z_T = 9.5H$ . The flux excited in the forcing zone is transported without loss to the top of the domain, where it is dissipated by the damping layer (see subsection 4.2) without reflection.

### 5.1 Numerical Simulation Results

A full video of our higher-resolution run at  $N_x = 1024, N_z = 4096$  can be found at<sup>3</sup>. Slices of  $\vec{U}, \hat{S}$  across  $z$  at various times  $t$  are shown in Figure 3. While the behavior of  $\vec{U}$  seems to conform qualitatively with the predictions of subsection 3.4, the behavior of  $\hat{S}$  exhibits two salient features: (i) the incident flux seems to fluctuate greatly with time, and (ii) there seems to be a small transmitted feature at many of the later times. We will discuss further these features in subsection 5.4, after first analyzing the propagation of the critical layer.

### 5.2 Propagating Critical Layer

For the simulation shown in Figure 3, we may analyze the location of the critical layer. As the simulations are very noisy, we define the location of the critical layer to be

$$\begin{aligned} z_{c,\min} &= \underset{z}{\operatorname{argmin}} \{z : S(z) < 0.3S_0\}, \\ z_{c,\max} &= \underset{z}{\operatorname{argmax}} \{z : S(z) > 0.3S_0\}, \\ z_c &\equiv \frac{z_{c,\min} + z_{c,\max}}{2}. \end{aligned} \quad (24)$$

This was found to a relatively stable estimator of the critical layer location. Other estimators were used and do not significantly change the results of the analysis.

The evolution of  $z_c$  is described by ODE Equation 18, and in the limit  $\Delta S(t) = \Delta S$  we obtained closed-form solution Equation 19. To estimate  $\Delta S(t)$  from the data, we defined:

$$S_{<}(t) = \langle S(z) \rangle_{z \in [z_c - \Delta z - H, z_c - \Delta z]}, \quad (25)$$

$$S_{>}(t) = \langle \{S(z) : S(z) < 0\} \rangle_{z \in [z_c, z_c + \Delta z]}, \quad (26)$$

$$\Delta S(t) \equiv S_{>}(t) - S_{<}(t). \quad (27)$$

$\langle \dots \rangle_{z \in [z_a, z_b]}$  denotes averaging over interval  $[z_a, z_b]$ . We average

<sup>3</sup> [http://www.princeton.edu/~lecoanet/data/breaking\\_wave.mov](http://www.princeton.edu/~lecoanet/data/breaking_wave.mov)



Name	Resolution	Re	$z$ spectral basis
Op5_hres	$512 \times 2048$	2048	Fourier
Op5_shres	$1024 \times 4096$	2048	Fourier
1_hres	$512 \times 2048$	1024	Fourier
1_vhres	$768 \times 3072$	1024	Fourier
2_hres	$512 \times 2048$	512	Fourier
3_width	$256 \times 1024$	341	Fourier
6_masked	$256 \times 1024$	512	Chebyshev
4_masked	$256 \times 1024$	341	Chebyshev
3_masked	$256 \times 1024$	205	Chebyshev
1_masked	$256 \times 1024$	146	Chebyshev

**Table 1.** Table of simulation parameters. Note that Re is defined as in Equation 23.

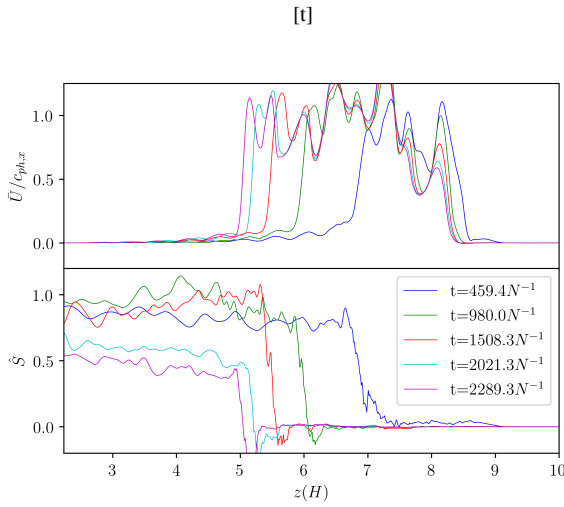


**Figure 3.** Plot of  $\bar{U}(z, t)$  and  $\hat{S}(z, t)$  respectively at various times over  $z$ .  $\bar{U}, \hat{S}$  follow their definitions in Equation 14 and Equation 22. The values are extracted from run Op5\_shres.  $\bar{U}$  is given in units of  $c_{ph,x} = \frac{\omega_1}{k_{1x}}$  the critical layer flow velocity (see subsection 3.4). The propagation of the critical layer towards lower  $z$  and sharp deposition of  $S$  at the critical layer are evident.

over an interval of length  $H = \frac{2\pi}{k_{1z}}$  a full vertical wavelength. The offset  $\Delta z$  is set by the observation that the critical layer's width is limited by  $Ri \lesssim 1$ , translating to a critical layer width of  $\sim \frac{1}{k_{1z}}$ . Here, we found  $\Delta z = \frac{3}{k_z}$  was necessary to be sufficiently offset from strong fluctuations near the critical layer.

Since the transmission feature can be seen in Figure 3 to attenuate rather quickly and is indeed rather weak, it is difficult to establish the correct interval to average over; we use the observation that  $S(z) < 0$  only for a small interval for  $z$  to select the interval length implicitly.

Finally, we may plot the observed  $z_c$  from data against two simple predictors: (i) integration of Equation 18 using the measured  $\Delta S(t)$ , and (ii) substituting the time-averaged  $\langle \Delta S \rangle_t$  into Equation 19. Since  $z_c(t)$  is both stable and less well-defined at early times (when the critical layer is thick and transient behavior is still strong), we instead integrate backwards from the end of the simulation, using  $z_c(t_f)$  as initial condition. The resulting predictors are depicted in Figure 4. The good agreement between the evolution of  $z_c(t)$  and its estimate via  $\Delta S(t)$  and Equation 18 are noteworthy. Further of interest is the discrepancy between the time-averaged predictor and the data. The general agreement clearly demonstrates  $\Delta S < S_1$  and that incomplete absorption is observed. Moreover, its significant un-

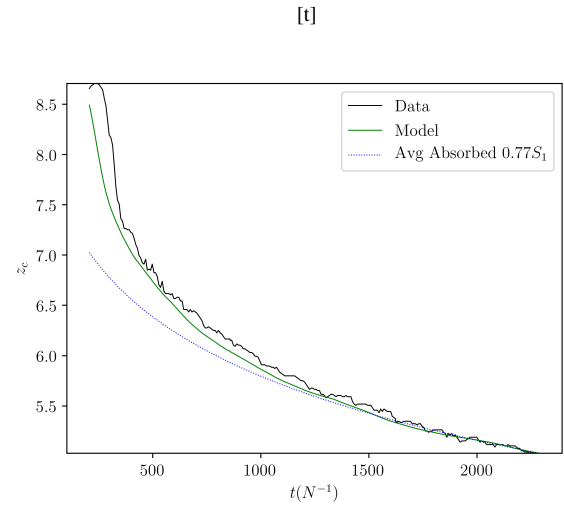


**Figure 4.** Propagation of the critical layer over time. Shown are (black)  $z_c(t)$  from simulation data, (green) predictor of  $z_c(t)$  using direct integration of Equation 18 for  $\Delta S(t)$  measured from simulation data (described in Equation 27) and (blue) direct substitution of time-averaged  $\langle \Delta S(t) \rangle_t$  into Equation 19. Predictors use the end of the simulation as initial conditions and integrate backwards, as  $z_c$  is less well-defined at early times. The agreement of the directly-integrated predictor with the data shows Equation 18 is a good description of the evolution of  $z_c$ . The poorer but qualitatively correct agreement of the time-averaged predictor with the data shows both that  $\Delta S(t) \neq S_1$  and that  $\Delta S(t)$  likely has some very real variation with time.

derprediction of critical layer motion at early times contrasts with its comparatively satisfactory prediction at later times to indicate that  $\Delta S(t)$  must vary significantly over time. Both of these observations indicate a careful characterization of reflectivity is necessary.

### 5.3 Kelvin-Helmholtz Instability and Critical Layer Width

The observation of reflected/transmitted waves is in accordance with previous studies as discussed in subsection 3.3. Many studies have shown that a local Richardson number  $Ri \sim 1/4$  corresponds to the onset of reflectivity. This agrees with the observed Kelvin-Helmholtz instability in our simulations [TODO image]. To verify that the critical layer's width is bound from below by Kelvin-Helmholtz instabilities, we decided to compute a  $Ri$  within the critical layer.

Since fluid instabilities are local,  $Ri$  must be measured in the immediate vicinity of a fluid parcel. Thus, we first assign an  $Ri$  for every  $x$  in the critical layer, then take the median as  $Ri$  for the entire layer. To avoid noisiness, the local  $Ri$  is computed using the vertical

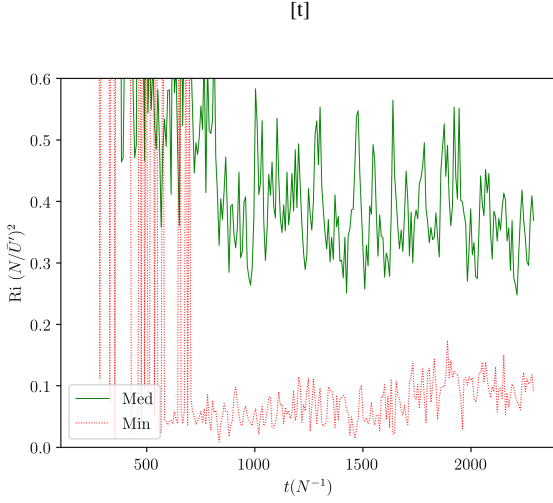


**Figure 5.** Local Richardson number of the flow at the critical layer over time as defined in Equation 28. Dotted red lines demarcate the minimum and maximum of Ri over  $x$  instead of the median. These numbers effectively measure the mean and spread in width of the critical layer over  $x$ . Note that  $Ri \lesssim \frac{1}{4}$  corresponds to Kelvin-Helmholtz instability, so this plot suggests the critical layer width roughly saturates the lower bound from the Kelvin-Helmholtz instability after an initial transient phase.

distance over which the local  $u_x$  increases from  $0.3 \times$  its critical value to its critical value. This can be written

$$\begin{aligned} z_{u,\min}(x, t) &= \operatorname{argmin}_{\zeta} \{z : u_x(x, \zeta, t) > 0.3\bar{U}_c\}, \\ z_{u,\max}(x, t) &= \operatorname{argmax}_{\zeta} \{z : u_x(x, \zeta, t) < \bar{U}_c\}, \\ Ri(t) &\equiv \operatorname{med}_x \left( \frac{N^2 (z_{u,\max} - z_{u,\min})^2}{(0.7\bar{U}_c)^2} \right). \end{aligned} \quad (28)$$

To understand the variation in Ri over  $x$ , we can also plot using the minimum over  $x$ ; the maximum is significantly noisier. Both of these are shown in Figure 5. The quick evolution of Ri to its saturated value is reflective of the fact that IGW are *anti-diffusive*. This property is a simple consequence of the IGW dispersion relation Equation 5, which is approximately  $\omega k_z \approx N k_x$  such that as an IGW propagates into a shear flow,  $\omega$  decreases and  $k_z$  increases, enhancing dissipation. Dissipation in a momentum-conserving fluid then corresponds to further mean flow acceleration.

#### 5.4 Non-absorption at Critical Layer

We identify two instances of non-absorptive behavior: (i), the presence of a reflected wave with wave vector  $\vec{k} = k_{1x}\hat{x} + k_{1z}\hat{z}$ , and (ii) the amount of horizontal momentum flux  $S$  reflected off the critical layer.

To measure the reflected wave amplitude, we use almost the same definition Equation 21 except using  $-k_{1z} \rightarrow +k_{1z}$ ; call this estimated  $\hat{A}_r(t)$  the amplitude of the downwards-propagating reflected wave, and call  $\hat{A}_i(t)$  the upwards-propagating incident wave. To compute  $\hat{A}_r(t)$ , we furthermore permit an arbitrary phase offset  $\phi_r(t)$  at each time  $t$ , since the phase of the reflected wave is unknown, unlike that of the incident wave. We observe that the evolution of  $\phi_r(t)$  is consistent with the interpretation of a reflected wave, as it is well approximated by  $\frac{\partial \phi_r}{\partial t} \approx 2 \frac{\partial(k_{1z} z_c)}{\partial t}$ , consistent with a wave reflecting off a moving boundary at  $z_c$ .

Since reflectivity depends sensitively on accurate measurements of  $\hat{A}_i, \hat{A}_r$ , it is important Equation 21 identically not pick up contributions between the two  $k_{1x}\hat{x} \pm k_{1z}\hat{z}$  modes, as we argued earlier. The integral for  $\hat{A}_r$  is also performed over  $z \in [z_0 + 3\sigma, z_0 + 3\sigma + H]$ . Since in general  $\hat{A}_i(t), \hat{A}_r(t)$  are functions of time, we must measure reflectivity accounting for propagation time between the measurement zone and the critical layer where the wave reflects. For some

$$\delta t(t) \approx \frac{z_c(t) - z_0 + 3\sigma + H/2}{c_{ph,z}}, \quad (29)$$

an incident wave measured at  $t - \delta t$  reflects at  $t$  and is re-measured as a reflected wave at  $t + \delta t$ . The choice of vertical phase velocity instead of group velocity is necessary to good results, and a possible explanation is provided in subsection 5.5. We can then define the amplitude reflectivity

$$\mathcal{R}_A(t) \equiv \frac{\hat{A}_r(t - \delta t)}{\hat{A}_i(t + \delta t)}. \quad (30)$$

Since in general  $\delta t$  can take on arbitrary values while  $\hat{A}_i, \hat{A}_r$  are sampled at discrete timesteps set by our simulation output, we evaluate  $\hat{A}_i, \hat{A}_r$  using a simple linear interpolation to intermediate times.

To measure the reflected horizontal momentum flux, we recall from our linear simulations described in subsection 4.3 that we are able to accurately predict the incident flux from the incident wave amplitude. Thus, we write for incident flux

$$S_i(t) \equiv \langle \rho u_{1x} u_{1z} \rangle_x \hat{A}_i^2(t). \quad (31)$$

But then, since we already have  $\Delta S(t), S_>(t)$  jump and transmitted flux across the critical layer at time  $t$  respectively, we can immediately write down the reflected flux

$$S_d(t) = S_i(t - \delta t) + \Delta S(t) - S_>(t). \quad (32)$$

$\delta t$  is still Equation 29; propagation time between  $z_c$  and  $z_c - 3/k_z - H/2$  the center averaging zone was ignored at the level of accuracy of the study. Then we can define flux reflectivity and transmissivity coefficients

$$\mathcal{R}_S(t) \equiv -\frac{S_d(t)}{S_i(t - \delta t)}, \quad \mathcal{T}_S(t) \equiv -\frac{S_>(t)}{S_i(t - \delta t)}. \quad (33)$$

The measurements of  $\hat{A}_i, \hat{A}_r, S_i, \Delta S, S_d, S_>$  are given in Figure 6. The oscillations in  $\hat{A}_i, S_i$  are evident and neatly correspond to oscillations in  $A_d, S_d$  respectively. We further analyze these oscillations in subsection 5.5.

Using these measured quantities, we may make plots of  $\mathcal{R}_A^2, \mathcal{R}_S, \mathcal{T}_S$ , which are provided in Figure 7. A comparison between  $\mathcal{R}_A^2$  and  $\mathcal{R}_S$  is appropriate as  $S \propto A^2$ . While less evident in the presented plot, a longer-duration simulation at lower resolution confirms that the three quantities have reached their asymptotic values after  $t \gtrsim 1750/N$ . An observation may be made that in general  $\mathcal{R}_S \geq \mathcal{R}_A^2$ ; this conforms to the intuition that reflected flux consists of the simple reflected mode and higher order modes as well.

Finally, we may be interested in the power spectrum of the transmitted horizontal momentum flux. Define:

$$\tilde{S}_>(k_x, t) = \left| \int_0^{L_x} e^{ik_x x} \hat{S}_>(x, z_c - \Delta z, t) dx \right|, \quad (34)$$

$$\tilde{S}_<(k_x, t) = \left| \int_0^{L_x} e^{ik_x x} \hat{S}_<(x, z_c + \Delta z, t) dx \right|. \quad (35)$$

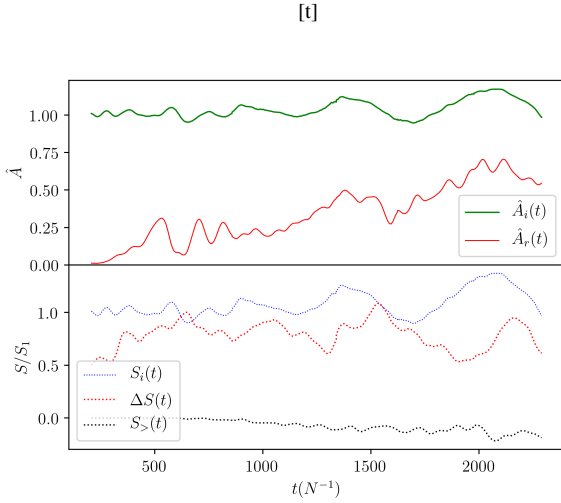


**Figure 6.** The top panel measures the incident wave amplitude  $\hat{A}_i(t)$  (green) and the downwards propagating wave amplitude  $\hat{A}_r(t)$  (red) just above the forcing zone, normalized to the analytical estimate Equation 12.  $A_d \neq 0$  due to reflection off the critical layer. The bottom panel shows the behavior of three horizontal momentum fluxes over time, in units of the analytical estimate Equation 10: (blue) flux incident on the critical layer, (red) flux absorbed by the critical layer, and (black) flux transmitted through the critical layer. Note that no propagation time effects have been included in these plots.

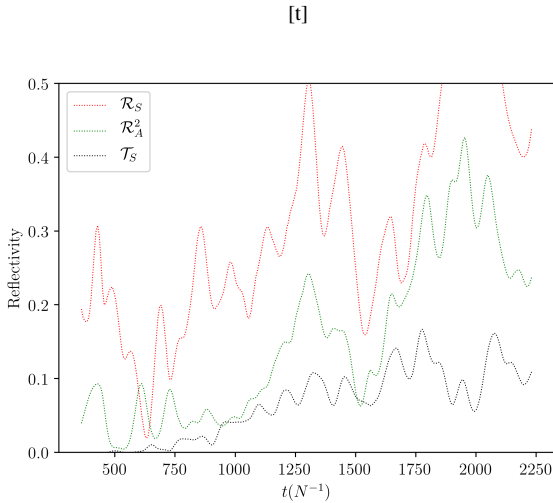


**Figure 7.** Reflectivity and transmittivity coefficients for flux and amplitude-squared as described by Equation 30 and Equation 33 respectively. The coefficients seem to become comparatively stable past about  $t = 1750/N$ , indicating that an asymptotic value may have been reached.

These values are plotted in Figure 8. Note that we expect  $\tilde{S}_<(0, t) = S_<(t) = S_i(t) + S_d(t)$  and the same for  $\tilde{S}_>$ . This is rather accurate for  $\tilde{S}_<$  but less so for  $\tilde{S}_>$ ; this is since  $S_>(t)$  decays very rapidly above  $z_c$ . Note furthermore that at later times, the transmitted flux increases, per expectation, and shifts towards higher  $k_x$ . Repeating this plot at higher viscosities shows significantly lower  $\tilde{S}_>$ , showing that the  $k_x$  of the transmitted waves still changes greatly at the highest Re we are able to probe. Finally, note that the area under  $\tilde{S}$  changes with time; this is okay since we are measuring  $S$  at constant

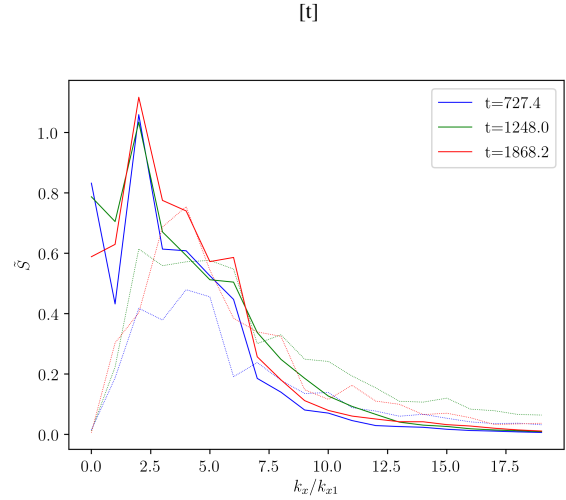


**Figure 8.** The power spectrum of the horizontal momentum flux at fixed distances below and above critical layer  $z_c$  at certain times  $t$  for simulation Op5\_shres. Equation 34 and Equation 35 are depicted here, with  $\tilde{S}_<$  in solid lines and  $\tilde{S}_>$  in dashed lines. Note that there is more incident flux than transmitted, and that transmitted flux roughly increases over time.

position, and different  $k_x$  components of  $S$  will translate at their separate group velocities.

### 5.5 Appearance of Discrete Modes

We briefly attribute the fluctuations in  $\hat{A}_i(t)$  as observed in Figure 6 to the introduction of discrete modes by partial reflection off a moving critical layer. The partially reflecting boundary causes a muted effect of the usual normal modes calculation, so a slightly stronger response  $\hat{A}_i > 1$  corresponds to being weakly on resonance. The instantaneous enhancement/attenuation of  $\hat{A}_i$  when  $z_c$  moves slowly can be computed by an overlap integral of the forcing with the modes of the finite domain. This is a consistent interpretation for three reasons:

- The period of the fluctuations in  $\hat{A}_i(t)$  grows longer at later times. This is consistent with  $\frac{\partial z_c}{\partial t}$  growing smaller at later times, as the critical layer propagates deeper (see Equation 18).
- The amplitude of the fluctuations in  $\hat{A}_i(t)$  grows larger at later times. This corresponds to the effective domain (below the critical layer) growing smaller, which leads to stronger effects.
- The propagation time  $\delta t$ , defined in Equation 29, used the vertical phase velocity instead of the vertical group velocity to obtain a non-oscillating reflectivity. This is consistent with the fluctuations in  $\hat{A}_i(t)$  being induced by internal modes of the domain rather than a varying forcing strength, as the latter should propagate at the *group velocity* instead.

### 5.6 Convergence

As the primary test of convergence in our previous sections, we consider the convergence of the physically significant parameters of our model. In particular, the convergence of Ri, shown in Figure 5, and of the reflection/transmission coefficient asymptotic values, shown in Figure 7, are of greatest significance.

To estimate convergence, we compute the median value of each of Ri,  $\mathcal{R}_A^2$ ,  $\mathcal{R}_S$ ,  $\mathcal{T}_S$  over the last 1/4 of simulation times from each



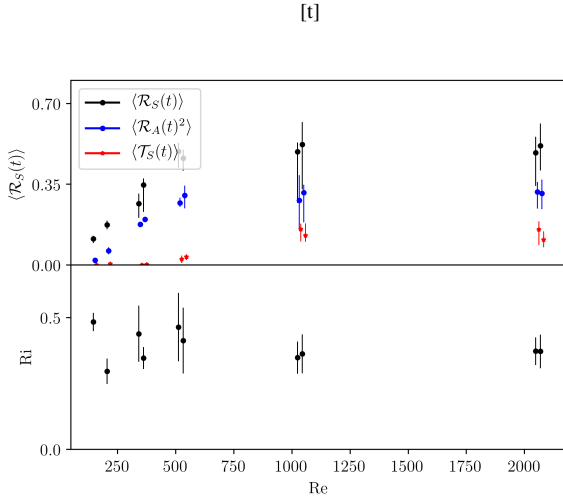


**Figure 9.** Convergence of median reflection/transmission coefficients and Ri (critical layer width) across runs with varying viscosity, parameterized with Re (Equation 23). Error bars depict 16 and 84 percentile values. Small horizontal displacements are made for data points at identical Re for readability. Note that simulations with larger Re correspond to smaller viscosity and are more physically realistic, and our values seem to converge towards large Re.

simulation, where all simulations had converged to what appeared to be asymptotic values. Error bars are estimated with the 16 and 84 percentiles. We illustrate the convergence of these averages across simulations in Figure 9.

## 6 DISCUSSION

In the previous section, we have argued for a continuous train of breaking IGWs spontaneously forming a critical layer and strong shear flow. We have parameterized the width of the critical layer as well as horizontal momentum transport near the critical layer. In the subsequent sections, we will discuss the validity of these results and their application to astrophysical systems.

### 6.1 Physical Sources of Dissipation in WDs

The most significant linear damping in WD g-modes comes from radiative damping (Fuller & Lai 2011). In (Wu 1998) and (Fuller & Lai 2011), the radiative damping rate is given in terms of  $\omega_i = \gamma\omega_r$ , where  $\omega_r$  is the frequency of the g-mode. Typical values for  $\gamma$  range from  $10^{-4}$  to  $10^{-11}$  depending on  $n$  of the g-mode.

We will assume this prescription directly transfers to propagating IGW, which results in general agreement with (Burkart et al. 2013)’s estimate of radiative damping rates. Then, making coarse identification  $\omega_i \sim \nu k^2 \approx \nu k_z^2$ , we find that  $\text{Re} \sim \frac{1}{\gamma}$ . Even at  $\gamma = 10^{-4}$  however, the corresponding Re is far too weak to suppress reflection/transmission at the critical layer (e.g. Figure 9).

Another source of dissipation considered in (Burkart et al. 2013) is turbulent convective damping. They find this damping rate to never exceed that of radiative damping, and so it is also too weak to suppress critical layer formation in our problem.

Finally, we consider the impact of magnetic winding. In (Burkart et al. 2013), magnetic winding is used to enforce solid

body rotation on the grounds that  $t_A \gg t_{gw}$ , where

$$t_A = \int_0^R \frac{\sqrt{4\pi\rho}}{B_0} dr \sim 10^2 \text{ yr} (*) \frac{10^3 \text{ G}}{B}. \quad (36)$$

the Alfvén wave crossing time (evaluated for a CO WD in (Fuller & Lai 2013)) measures the magnetic coupling time and  $t_{gw}$  measures the gravitational wave inspiral timescale. Before solid body rotation is attained, another relevant timescale is the synchronization timescale  $t_s$ . For a tidal torque  $\tau$  and tidal forcing frequency  $\sigma = m(*)\Omega - \Omega_{spin}$ , we note that angular momentum transfer is  $\frac{\partial M_{sync}}{\partial t} \sigma R^2 = \tau$ , where  $M_{sync}$  denotes the mass of the WD that has synchronized. Thus, the synchronization timescale is

$$t_{sync} \sim \frac{M_{sync} \sigma R^2}{\tau}, \\ \sim 2 \times 10^5 \text{ yr} \left( \frac{M}{M_\odot} \right) \left( \frac{\sigma}{2\pi/(1 \text{ hr})} \right) \left( \frac{R}{R_\oplus} \right)^2 \left( \frac{10^{-14} GM_\odot^2/R_\oplus}{\tau} \right). \quad (37)$$

A representative  $\tau$  has been taken from (Burkart et al. 2013). However, since only the outer  $\sim 10^{-4} M_\odot$  need be heated for the thermodynamically interesting effects studied in (Fuller & Lai 2013) and (Fuller & Lai 2012b), it seems that magnetic winding cannot absolutely rule out energetic outbursts such as tidal novae resulting from strong shear flows.

### 6.2 Applicability to Other Astrophysical Systems

[TODO flesh out]

- $k_x, k_z$ : In astrophysical systems,  $k_\perp \ll k_r$ . While we do not explore different  $k_{1x}, k_{1z}, \omega_1$  in this study, with outgoing boundary conditions, there appears at first to be no  $z$  length scale other than  $k_{1z}$ , so our results would seem to be invariant under rescaling of the  $z$  length scale. However, true turbulence is expected to be isotropic at small scales, which may couple  $k_{1x}, k_{1z}$  in a way that  $k_{1x} \ll k_{1z}$  produces different dynamics than  $k_{1x} \lesssim k_{1z}$  as we’ve studied. This is a numerically difficult regime though, so we defer consideration to future work.

- Validity of plane-parallel approximation? We’re all at  $\geq 0.9R_{WD}$ .

- Solar-type stars (inner convective, outer radiative): different equation of state/stratification but could be qualitatively similar.

- Solar-type stars: In Barker & Ogilvie (2010), inwards-propagating IGW are excited that break via geometric focusing and effect synchronization. They find no reflected wave despite their nonlinear timescales being 10× shorter than their viscous timescale.

It is not immediately clear whether our results here apply when the flux is geometrically focused, but as a hypothesis we assume the convergence in Figure 9 applies under geometric focusing as a zeroth approximation, perhaps as a property of the fluid motion within the geometrically thin critical layer.

Associating  $t \sim \nu k^2 \approx \nu k_z^2$  with the viscous timescale and  $t_{NL} \sim \vec{u} \cdot \vec{\nabla} \sim \omega$  for the nonlinear timescale, we find their  $\lambda = \frac{t_{NL}}{t_L} \sim \text{Re}$  our Reynolds number. Our simulations indicate  $\text{Re} \gtrsim 500$  are required to observe the correct asymptotic behavior in terms of horizontal momentum flux reflection/transmission, so it is possible their lack of reflection is viscosity limited.

### 6.3 Heating

[TODO elaborate? Need to make plots to check?]

Our equations do not conserve energy, but it seems like more energy can be transmitted in higher modes as viscosity is decreased. Nevertheless, a significant fraction should still be dissipated in the critical layer since a significant energy cascade must happen in the critical layer.

## 7 ACKNOWLEDGEMENTS

### REFERENCES

- Andrews D., McIntyre M. E., 1976, *Journal of the Atmospheric Sciences*, 33, 2031
- Ascher U. M., Ruuth S. J., Spiteri R. J., 1997, *Applied Numerical Mathematics*, 25, 151
- Barker A. J., Ogilvie G. I., 2010, *MNRAS*, 404, 1849
- Booker J. R., Bretherton F. P., 1967, *J. Fluid Mech.*, 27, 513–539
- Boyd J. P., 2001, *Chebyshev and Fourier spectral methods*. Courier Corporation
- Brown S., Stewartson K., 1982, *Journal of Fluid Mechanics*, 115, 217
- Burkart J., Quataert E., Arras P., Weinberg N. N., 2013, *Monthly Notices of the Royal Astronomical Society*, 433, 332
- Burns K. J., Vasil G. M., Oishi J. S., Lecoanet D., Brown B., 2016, *Dedalus: Flexible framework for spectrally solving differential equations*, *Astrophysics Source Code Library* (ascl:1603.015)
- Dosser H. V., Sutherland B. R., 2011a, *J. Atmos. Chem.*, 68, 2844
- Dosser H., Sutherland B., 2011b, *Physica D: Nonlinear Phenomena*, 240, 346
- Drazin P., 1977, *Proc. R. Soc. Lond. A*, 356, 411
- Fuller J., Lai D., 2011, *MNRAS*, 412, 1331
- Fuller J., Lai D., 2012a, *MNRAS*, 421, 426
- Fuller J., Lai D., 2012b, *ApJL*, 756, L17
- Fuller J., Lai D., 2013, *MNRAS*, 430, 274
- García-Berro E., Badenes C., Aznar-Siguán G., Lorén-Aguilar P., 2017, *MNRAS*, 468, 4815
- Gilfanov M., Bogdán Á., 2010, *Nature*, 463, 924
- Goldreich P., Nicholson P. D., 1989, *ApJ*, 342, 1079
- Hazel P., 1967, *J. Fluid Mech.*, 30, 775–783
- Iben Jr I., Tutukov A. V., 1984, *ApJS*, 54, 335
- Kilic M., Hambly N. C., Bergeron P., Genest-Beaulieu C., Rowell N., 2018, *MNRAS*, 479, L113
- Klostermeyer J., 1991, *Geophysical & Astrophysical Fluid Dynamics*, 61, 1
- Korol V., Rossi E. M., Groot P. J., Nelemans G., Toonen S., Brown A. G. A., 2017, *MNRAS*, 470, 1894
- Lecoanet D., Vasil G. M., Fuller J., Cantiello M., Burns K. J., 2016, *Monthly Notices of the Royal Astronomical Society*, 466, 2181
- Lindzen R. S., Holton J. R., 1968, *Journal of the Atmospheric Sciences*, 25, 1095
- Maoz D., Sharon K., Gal-Yam A., 2010, *ApJ*, 722, 1879
- Nelemans G., 2009, *Class. Quantum Grav.*, 26, 094030
- Perets H. B., et al., 2010, *Nature*, 465, 322
- Shen K. J., et al., 2018, *AJ*, 865, 15
- Webbink R., 1984, *ApJ*, 277, 355
- Winters K. B., D’Asaro E. A., 1994, *J. Fluid Mech.*, 272, 255–284
- Wu Y., 1998, PhD thesis, California Institute of Technology
- Zahn J.-P., 1975, *A&A*, 41, 329

## APPENDIX A: EQUATION IMPLEMENTATIONS

We denote  $x \in [0, L_x], z \in [0, L_z]$  the simulation domain and  $N_x, N_z$  the number of spectral modes in the respective dimensions.

Numerically, the nonlinear  $\frac{\vec{\nabla} P}{\rho}$  term is problematic: we desire a system where the fluid fields are not divided by one another. We introduce  $\varpi = \frac{P}{\rho}$  instead, then mandate  $\rho_0, \varpi_0$  background fields satisfy hydrostatic equilibrium  $\vec{\nabla} \varpi_0 + \varpi_0 \vec{\nabla} \rho_0 + g \hat{z} = 0$ . Taking isothermal stratification, we find  $\varpi_0 = gH$ . We further change variables to  $\Upsilon = \ln \rho - \ln \rho_0$  and  $\varpi_1 = \varpi - \varpi_0$  deviations from the background state to obtain a system of equations at most quadratic in fluid fields:

$$\vec{\nabla} \cdot \vec{u}_1 = 0, \quad (\text{A1a})$$

$$\frac{\partial \Upsilon}{\partial t} + (\vec{u}_1 \cdot \vec{\nabla}) \Upsilon - \frac{u_z}{H} = 0, \quad (\text{A1b})$$

$$\frac{\partial u_{1x}}{\partial t} + (\vec{u}_1 \cdot \vec{\nabla}) u_{1x} + \frac{\partial \varpi_1}{\partial x} + gH \frac{\partial \Upsilon}{\partial x} + \varpi_1 \frac{\partial \Upsilon}{\partial x} = 0, \quad (\text{A1c})$$

$$\frac{\partial u_z}{\partial t} + (\vec{u}_1 \cdot \vec{\nabla}) u_z + \frac{\partial \varpi_1}{\partial z} + gH \frac{\partial \Upsilon}{\partial z} + \varpi_1 \frac{\partial \Upsilon}{\partial z} - \frac{\varpi_1}{H} = 0. \quad (\text{A1d})$$

It bears noting that these equations are exactly equivalent to the original Euler equations and hence conserve horizontal momentum.

### A1 Artificial Dissipation

The nonlinear terms in the above equations will transfer energy from lower wavenumbers to higher wavenumbers. Since spectral codes have no numerical dissipation, artificial dissipation must be added. To ensure the dissipative system conserves horizontal momentum, we begin by adding dissipative terms to the flux-conservative form of the Euler fluid equations [Equation 1](#) (we use stress tensor  $\tau_{ij} = P\delta_{ij}$ ):

$$\vec{\nabla} \cdot \vec{u} = 0, \quad (\text{A2a})$$

$$\partial_t \rho + \vec{\nabla} \cdot (\rho \vec{u} - \nu \vec{\nabla}(\rho - \rho_0)) = 0, \quad (\text{A2b})$$

$$\partial_t (\rho \vec{u}) + \vec{\nabla} \cdot (\rho \vec{u} \vec{u} + \text{diag}(\rho \varpi) - \nu \rho \vec{\nabla} \vec{u}) + \rho g \hat{z} = 0. \quad (\text{A2c})$$

The same  $\nu$  is used for both the diffusive and viscous term, though this is not required. Since the dissipation is not physical and is purely used for numerical stability, we choose it such that hydrostatic equilibrium is not modified. Some algebraic manipulation to re-cast it in the form of [Equation A1](#) gives

$$\vec{\nabla} \cdot \vec{u} = 0, \quad (\text{A3a})$$

$$\partial_t \Upsilon + (\vec{u} \cdot \vec{\nabla}) \Upsilon - \frac{u_z}{H} - \nu \left( \nabla^2 \Upsilon + (\vec{\nabla} \Upsilon) \cdot (\vec{\nabla} \Upsilon) - \frac{2}{H} \partial_z \Upsilon + \frac{1 - e^{-\Upsilon}}{H^2} \right) = 0, \quad (\text{A3b})$$

$$\begin{aligned} \partial_t \vec{u} + (\vec{u} \cdot \vec{\nabla}) \vec{u} + \vec{\nabla} \varpi + \varpi \vec{\nabla} \Upsilon - \nu \nabla^2 \vec{u} + \vec{u} \nu \left( \nabla^2 \Upsilon + (\vec{\nabla} \Upsilon) \cdot (\vec{\nabla} \Upsilon) - \frac{2}{H} \partial_z \Upsilon + \frac{1 - e^{-\Upsilon}}{H^2} \right) \\ - 2\nu \left( ((\vec{\nabla} \Upsilon) \cdot \vec{\nabla}) \vec{u} - \frac{1}{H} \partial_z \vec{u} \right) - \frac{\varpi_1}{H} = 0. \end{aligned} \quad (\text{A3c})$$

Hydrostatic equilibrium is still  $\vec{\nabla} \varpi_0 + g \hat{z} = 0$  where  $\rho = \rho_0, \vec{u} = 0$ . Including the damping layers and forcing terms as described in [subsection 4.1](#), we finally obtain the full system of equations as simulated in Dedalus: [TODO update w/ mask]

$$\vec{\nabla} \cdot \vec{u} = 0, \quad (\text{A4a})$$

$$\begin{aligned} \partial_t \Upsilon - \frac{u_z}{H} = \nu \left( \nabla^2 \Upsilon + (\vec{\nabla} \Upsilon) \cdot (\vec{\nabla} \Upsilon) - \frac{2}{H} \partial_z \Upsilon + \frac{1 - e^{-\Upsilon}}{H^2} \right), \\ - (\vec{u} \cdot \vec{\nabla}) \Upsilon - \Gamma(z) \Upsilon + \frac{F}{\rho_0(z)} e^{-\frac{(z-z_0)^2}{2\sigma^2}} \cos(k_x x - \omega t), \end{aligned} \quad (\text{A4b})$$

$$\begin{aligned} \frac{\partial u_x}{\partial t} + \frac{\partial T}{\partial x} + gH \frac{\partial \Upsilon}{\partial x} = \nu \nabla^2 u_x - u_x \nu \left( \nabla^2 \Upsilon + (\vec{\nabla} \Upsilon) \cdot (\vec{\nabla} \Upsilon) - \frac{2}{H} \partial_z \Upsilon + \frac{1 - e^{-\Upsilon}}{H^2} \right) \\ + 2\nu \left( ((\vec{\nabla} \Upsilon) \cdot \vec{\nabla}) u_x - \frac{1}{H} \partial_z u_x \right) - \Gamma(z) u_x - (\vec{u} \cdot \vec{\nabla}) u_x - T_1 \frac{\partial \Upsilon}{\partial x}, \end{aligned} \quad (\text{A4c})$$

$$\begin{aligned} \frac{\partial u_z}{\partial t} + \frac{\partial T}{\partial z} + gH \frac{\partial \Upsilon}{\partial z} - \frac{T_1}{H} = \nu \nabla^2 u_z - u_z \nu \left( \nabla^2 \Upsilon + (\vec{\nabla} \Upsilon) \cdot (\vec{\nabla} \Upsilon) - \frac{2}{H} \partial_z \Upsilon + \frac{1 - e^{-\Upsilon}}{H^2} \right) \\ + 2\nu \left( ((\vec{\nabla} \Upsilon) \cdot \vec{\nabla}) u_z - \frac{1}{H} \partial_z u_z \right) - \Gamma(z) u_z - (\vec{u} \cdot \vec{\nabla}) u_z - T_1 \frac{\partial \Upsilon}{\partial z}. \end{aligned} \quad (\text{A4d})$$